Ensemble Simulations of the 2012 July 12 Coronal Mass Ejection with the Constant-turn Flux Rope Model

Talwinder Singh[1] , Tae K. Kim[1] , Nikolai V. Pogorelov[1,2] , and Charles N. Arge[3]

[1] Center for Space Plasma and Aeronomic Research, The University of Alabama in Huntsville, Huntsville, AL 35805, USA; talwinder.singh@uah.edu
[2] Department of Space Science, The University of Alabama in Huntsville, Huntsville, AL 35805, USA
[3] Solar Physics Lab, NASA/GSFC, Greenbelt, MD 20771, USA

Abstract

Flux-rope-based magnetohydrodynamic modeling of coronal mass ejections (CMEs) is a promising tool for prediction of the CME arrival time and magnetic field at Earth. In this work, we introduce a constant-turn flux rope model and use it to simulate the 2012 July 12 16:48 CME in the inner heliosphere. We constrain the initial parameters of this CME using the graduated cylindrical shell (GCS) model and the reconnected flux in post-eruption arcades. We correctly reproduce all the magnetic field components of the CME at Earth, with an arrival time error of approximately 1 hr. We further estimate the average subjective uncertainties in the GCS fittings by comparing the GCS parameters of 56 CMEs reported in multiple studies and catalogs. We determined that the GCS estimates of the CME latitude, longitude, tilt, and speed have average uncertainties of $5°.74$, $11°.23$, $24°.71$, and 11.4%, respectively. Using these, we have created 77 ensemble members for the 2012 July 12 CME. We found that 55% of our ensemble members correctly reproduce the sign of the magnetic field components at Earth. We also determined that the uncertainties in GCS fitting can widen the CME arrival time prediction window to about 12 hr for the 2012 July 12 CME. On investigating the forecast accuracy introduced by the uncertainties in individual GCS parameters, we conclude that the half-angle and aspect ratio have little impact on the predicted magnetic field of the 2012 July 12 CME, whereas the uncertainties in longitude and tilt can introduce relatively large spread in the magnetic field predicted at Earth.

Unified Astronomy Thesaurus concepts: Solar coronal mass ejections (310); Solar wind (1534)

1. Introduction

Coronal mass ejections (CMEs) are plasma and magnetic field structures that usually erupt from highly magnetic, closed-field regions of the Sun called active regions (ARs). CMEs can carry large kinetic and magnetic energy, with their erupted mass ranging between 10^9 and 10^{13} kg (Vourlidas et al. 2010) and speeds that may exceed 3000 km s^{-1}. When CMEs travel through the interplanetary space, they are referred to as interplanetary CMEs (ICMEs). An Earth-directed ICME carrying a negative out-of-ecliptic magnetic field component (B_z) can cause extreme space weather events that can affect space-borne and ground-based technological systems. Therefore, predicting ICME arrival times and magnetic field values at Earth by properly treating their interplanetary propagation is of immense importance.

A number of ICME propagation models have been developed over the years to reproduce their travel through interplanetary space and forecast arrival times at Earth. Such models include empirical models (e.g., Vandas et al. 1996; Brueckner et al. 1998; Gopalswamy et al. 2001, 2005; Wang et al. 2002), drag-based models (DBMs; Vršnak & Gopalswamy 2002), and physics-based models, such as the shock time of arrival (STOA; Dryer & Smart 1984), STOA-2 (Moon et al. 2002), and HAFv.2 (Fry et al. 2001). Newer-generation prediction models such as the Wang-Sheeley-Arge (WSA)-ENLIL-Cone model (Odstrcil et al. 2004) use magnetohydrodynamic (MHD) simulations in which ICMEs are inserted into the ambient flow as nonmagnetized

overpressured plasma blobs. The accuracy of these types of models is not much higher than in the previously mentioned models of lesser complexity and have a mean absolute error of more than 10 hr (Amerstorfer et al. 2018; Riley et al. 2018). Gopalswamy et al. (2013) have shown that the performance of the WSA-ENLIL-Cone model is similar to that of the empirical shock arrival model (Gopalswamy et al. 2005). The WSA-ENLIL-Cone and HAFv.2 models can calculate magnetic field in the ICME sheath region because a preceding shock distorts the interplanetary magnetic field. However, they are unable to describe magnetic field in ICME clouds at Earth because of the absence of an explicitly defined magnetic field inside them (Fry et al. 2001; Odstrcil et al. 2004). Attempts have been made to remedy this by adding a simple magnetic field into the plasma blobs (see, e.g., Shen et al. 2011).

According to the standard model of CME eruption, also called the CSHKP model (Carmichael 1964; Sturrock 1968; Hirayama 1974; Kopp & Pneuman 1976), preeruptive states are characterized by the presence of an axial magnetic flux, which may be either a sheared arcade or a flux rope located above the magnetic polarity inversion line separating positive and negative radial magnetic fluxes in an AR. Such flux ropes can rise owing to different magnetic force imbalances, and the overlying magnetic field lines add the majority of poloidal flux to the flux rope during an eruption (see the review of Chen 2011). The interplanetary counterparts of CME flux ropes that are characterized by a large, rotating magnetic field, as revealed by in situ measurements, are called the magnetic clouds (Burlaga et al. 1981).

Using in situ observations of ICMEs between 1978 and 1982, Gosling (1990) showed that $\sim 30\%$ of ICMEs sampled at 1 au had magnetic clouds associated with them. However,

Marubashi (2000) later claimed that up to 80% of all ICMEs involve magnetic clouds. A recent study by Song et al. (2020) argues that all CMEs observed at 1 au have magnetic clouds, though some are not directly observed because the observing spacecraft crosses the flanks of the ICME. Studies such as Gopalswamy et al. (2018a) and Sarkar et al. (2020) show the key importance of flux ropes in the development of forecast models capable of predicting the CME magnetic properties at 1 au. Therefore, the new generation of CME forecast models is strongly associated with the advanced description of flux rope structures (Shen et al. 2011; Shiota & Kataoka 2016; Isavnin 2016; Jin et al. 2017; Vandas & Romashets 2017; Scolini et al. 2019; Singh et al. 2020).

MHD simulations of the solar wind (SW) and flux-rope-based CMEs can start in either the lower corona (Manchester et al. 2004; Jin et al. 2016; Singh et al. 2018) or the inner heliosphere (IH; Verbeke et al. 2019; Singh et al. 2020). If a simulation starts in the lower corona, one can allow a CME to be automatically generated in the ambient solar corona background (Amari et al. 2014). Otherwise, an analytically generated flux rope can be inserted (Titov & Démoulin 1999; Gibson & Low 1998; Singh et al. 2020). The latter approach is less computationally expensive than the former and allows for better constraining of magnetic flux inside flux rope models (Singh et al. 2019). The approach where CMEs are inserted in the IH is computationally less expensive and easier to implement since the boundary condition treatment in the superfast magnetosonic flow is mathematically trivial and no coronal heating model is required. However, this approach can lead to errors associated with the extrapolation of the SW and CMEs from the lower corona to the inner boundary of the IH models. This approach is more common to the current operational ICME predictions such as by the NASA Goddard Space Flight Center/Space Weather Research Center, NOAA/Space Weather Prediction Center USA, Australian Bureau of Meteorology, Korean Space Weather Center, and UK Met Office, which use the WSA-ENLIL-Cone model. This approach is also being pursued by several other models, e.g., EUHFORIA (Verbeke et al. 2019) and the one described by Shiota & Kataoka (2016).

In an IH model, a CME can be inserted either step by step at the inner boundary (Verbeke et al. 2019) or in a single step above the inner boundary (Singh et al. 2020). If a CME flux rope is inserted by superimposing an analytic model either in the corona or in the IH, its physical and magnetic properties should be driven by observations for accurate forecasting. These properties include the CME direction, tilt, shape, speed, mass, poloidal and toroidal magnetic fluxes, and helicity sign. The CME tilt refers here to the angle between the line connecting two footpoints of the CME flux rope and the equatorial plane. This tilt can be seen as angle γ in Figure 1 of Thernisien et al. (2009). Moreover, the ambient SW through which this CME will propagate should also be based on data-driven models. CME observations used to constrain any model are typically accompanied by uncertainties in different measured quantities. It is crucial to understand how these uncertainties propagate through the computational region and affect the model forecasts at Earth. Ensemble modeling of CMEs is a viable approach to the study of the propagation of these uncertainties and ensures the probabilistic forecasting (Pizzo et al. 2015; Mays et al. 2015; Murray 2018; Amerstorfer et al. 2021).

In this paper, we use the constant-turn flux rope model to simulate a CME that erupted on 2012 July 12 at 16:48. The geometry of this model is described by the FRiED model of Isavnin (2016). We use the analytic formulae governing the constant-turn flux rope, as described by Vandas & Romashets (2017), to specify the magnetic field in this model. We estimate the 2012 July 12 CME direction, tilt, half-angle, aspect ratio, and speed using the graduated cylindrical shell (GCS) model and initialize our flux rope using these properties. The magnetic flux associated with a CME in the flux rope model is calculated using the poloidal flux estimated from post-eruption arcades (PEAs).

We demonstrate that by using these observational initial conditions it is possible to correctly reproduce the sign of all three magnetic field components of the magnetic cloud of this ICME. The arrival time, density, and speed are also reproduced with reasonably good accuracy as compared to previous attempts to simulate this CME using different models (Shen et al. 2014; Scolini et al. 2019; Singh et al. 2020). We also perform an analysis of differences in GCS fitting results reported in multiple publications and online catalogs to quantify the uncertainties associated with such fittings. We further investigate how the uncertainties in the GCS parameters, both individually and collectively, affect the simulated CME properties at Earth by using an ensemble modeling of the 2012 July 12 CME.

In Section 2, we describe the GCS model, the SW model, and the flux-rope-based CME model. We then show our CME simulation and GCS uncertainty analysis results in Section 3, followed by the conclusions in Section 4.

2. Data and Models

In this work, we use the level 0.5 image data collected on 2012 July 12 between 16:24 and 18:54 UT from the Sun−Earth Connection Coronal and Heliospheric Investigation (SEC-CHI)/Cor2 (Howard et al. 2008) coronagraphs on board the STEREO-A and STEREO-B (Kaiser et al. 2008) spacecraft and process them to level 1 using the *secchi_prep* program in the IDL SolarSoft library, which converts the units from data numbers (DN) into Mean Solar Brightness (MSB). We also use level 1 image data collected on 2012 July 12 between 16:24 and 17:18 UT from the Large Angle Spectroscopic Coronagraph (LASCO)/C2/C3 (Brueckner et al. 1995) coronagraph of the Solar and Heliospheric Observatory (SOHO) spacecraft. Level 1 data for both these instruments are suitable for quantitative scientific analysis. The coronagraph data are used to estimate the speed, direction, tilt, half-angle, aspect ratio, and speed of the 2012 July 12 CME. The model used to estimate these values is described in Section 2.1. We use the solar extreme-ultraviolet (EUV) images in 94, 131, and 193 Å wavelengths captured on 2012 July 12 at 22:30 UT and line-of-sight (LOS) magnetic field observations at 2012 July 12 16:10 UT from Solar Dynamics Observatory's (SDO) Atmospheric Imaging Assembly (AIA; Pesnell et al. 2012) and Helioseismic and Magnetic Imager (HMI; Schou et al. 2012; Hoeksema et al. 2014), respectively. We use the *aia_prep* program in SolarSoft to read in and calibrate AIA level 1 data to level 1.5. Level 1 data include bad-pixel removal, de-spiking, and flat-fielding. Additional roll corrections applied to level 1.5 data make the solar north direction vertical in the images, rescale the images to 0″.6 pixels, and translate them to match the solar disk and image centers. The
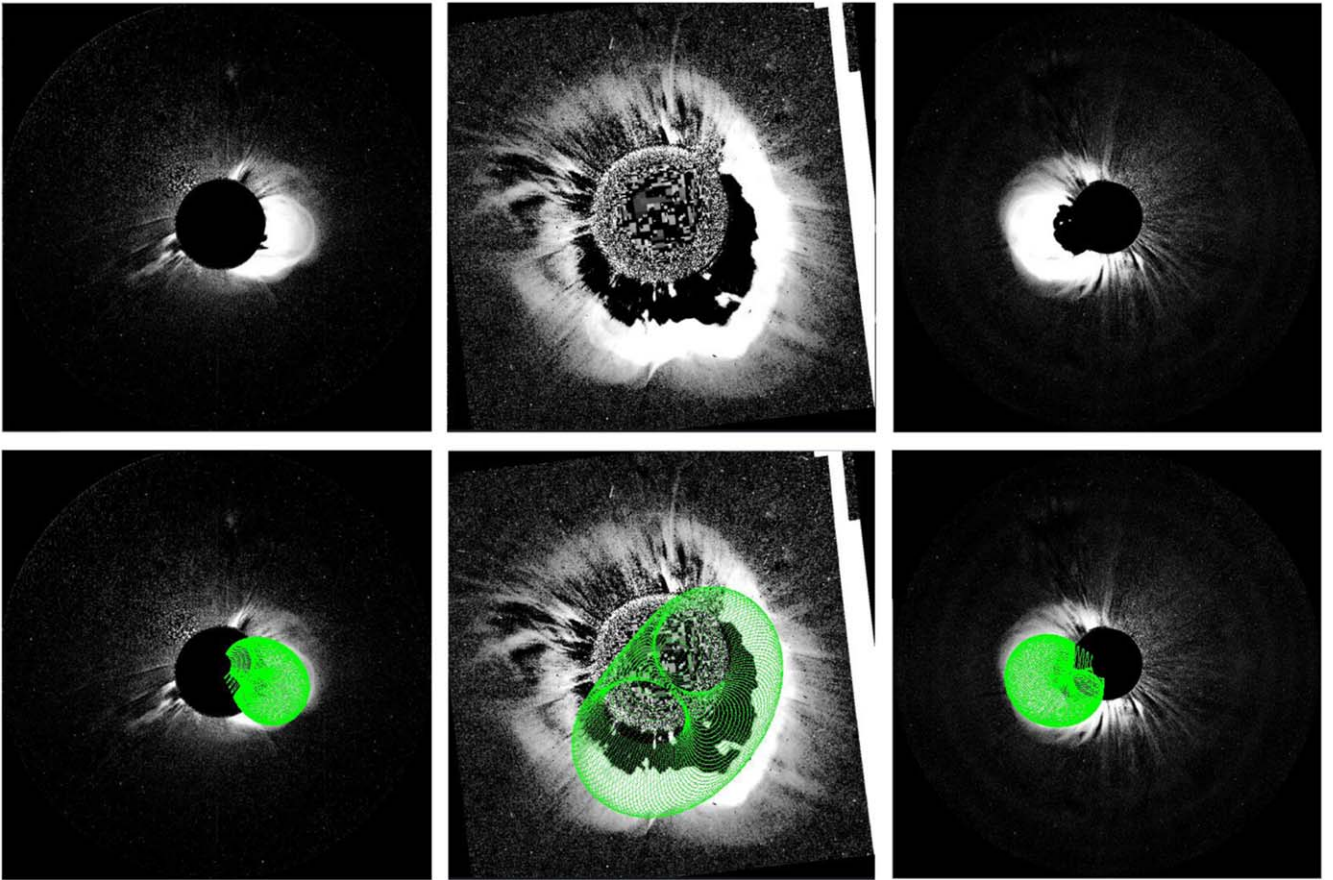
Figure 1. Top panels, from left to right: the 2012 July 12 CME seen in STEREO-B Cor2, SOHO C2, and STEREO-A Cor2 coronagraphs, respectively. Bottom panels: the same CME, but fitted with the GCS model.

HMI data are read using the *hmi_prep* program in SolarSoft, which processes magnetograms to ensure correct roll angles and translates them to put the solar disk center at a magnetogram center. These data are used to estimate the magnetic flux and helicity sign of the 2012 July 12 CME. The methods used to estimate these values are described in Section 3.1. We use 1 hr averaged data provided by NASA/GSFC's OMNI data set through OMNIWeb (King & Papitashvili 2005) to compare the in situ properties at Earth with our simulations of 2012 July 12 CME.

2.1. Graduated Cylindrical Shell Model

The GCS model uses three different views of a CME from STEREO-A, STEREO-B, and SOHO coronagraphs to visually fit the observed CME with a simplified structure consisting of conical legs and a curved front, resembling a hollow croissant with a circular cross section. The GCS method has been implemented in IDL using the *rtsccguicloud* program (Thernisien et al. 2006). An example of GCS fitting using this tool is shown in Figure 1, for the 2012 July 12 CME. The GCS model has six free parameters, namely, the latitude, longitude, tilt, height, half-angle, and aspect ratio, which can be modified to fit the 3D flux rope structure in all three images simultaneously. The *rtsccguicloud* program allows for this modification by using sliders to modify each parameter independently. The mathematical description of the geometry of this model is described in detail by Thernisien (2011). Notice that the CME height, being one of the GCS parameters, can be converted to speed by fitting a linear function

to the height−time graph. We decided to use linear fitting instead of quadratic fitting because the GCS uncertainty analysis we perform later in the study is based on the catalogs that all reported only the linear speeds. One cannot reliably derive GCS parameters with a single coronagraph image, since the majority of structural information of a CME is lost when its 3D shape is projected onto a 2D plane (plane of the sky). The availability of multiple images made from different viewpoints is critical for our ability to remove these projection effects. However, CMEs typically have complicated shapes that are difficult to fit with the idealized shapes assumed by the GCS model. Therefore, the CME parameters estimated by the GCS model can have significant uncertainties. We will discuss them in more detail in Section 3.2.

2.2. Magnetohydrodynamic Models

In this study, we perform MHD modeling using the Multi-Scale Fluid-Kinetic Simulation Suite (MS-FLUKSS), a collection of highly parallel modules capable of performing adaptive mesh refinement (AMR) simulations of the SW in the presence of neutral atoms, nonthermal ions, turbulence, etc. (Pogorelov et al. 2014). We describe our SW and CME models in the following subsections.

2.2.1. Solar Wind Model

We simulate the ambient SW in the IH by solving the ideal MHD equations with the finite-volume, total variation diminishing (TVD) approximation on a nonuniform spherical grid with 150, 256, and 128 cells in the r-, ϕ-, and θ-directions,
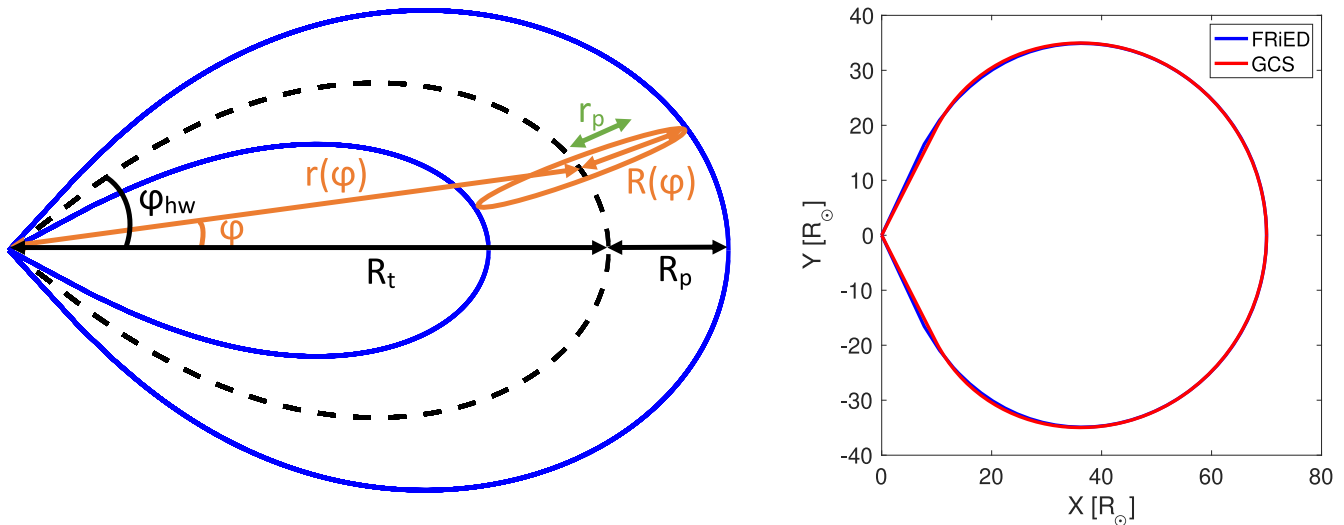
Figure 2. Left panel: a cross section of constant-turn flux rope by the plane containing the curved axis of this flux rope (shown here by the dashed black line). Blue lines represent the inner and outer edges of the flux rope in this plane. The variable $r(\phi)$ is a polar coordinate describing the curved axis. $R(\phi)$ is the radius of the out-of-plane circular cross section (shown with orange color) centered at a point belonging to the curved axis, while r_p is the distance of a point on this circular cross section from its center. $R(\phi)$ and $r(\phi)$ are given by Equations (1) and (2) respectively. Right panel: the outer edge of the FRiED model with model parameters $R_t = 46.67R_\odot$, $R_p = 23.33R_\odot$, $\phi_{\rm hw} = 40°$, and $n = 0.33$ compared with the outer edge of the GCS model with model parameters half-width $= 33°$, height $= 70\,R_\odot$, and aspect ratio $= 0.5$.

respectively. We set the inner and outer boundaries of the spherical domain at 0.1 and 1.5 au, respectively. The IH model uses a time series of WSA maps as inner boundary conditions at 0.1 au (e.g., Kim et al. 2020). We employ the Air Force Data Assimilative Photospheric Flux Transport (ADAPT) synchronic maps using the NSO/GONG magnetograms (Arge et al. 2010, 2011, 2013; Hickmann et al. 2015) as input to the WSA model at the solar surface. The WSA model extrapolates the photospheric magnetic field to a spherical source surface at 2.5 $R_\odot$ using the potential field source surface (PFSS) model and then to the WSA outer boundary at 0.1 au using the Schatten current sheet model (Schatten 1971). The WSA model also calculates the SW speed at its outer boundary as a function of the flux expansion factor and distance to the nearest coronal hole boundary (Arge et al. 2003, 2005; McGregor et al. 2011). To generate the background SW for the flux rope CME, we use the best ADAPT-WSA realization (out of 12), based on their comparison with near-Earth SW data.

We interpolate the WSA maps, in both time and space, from the original 2°.5 × 2°.5 resolution to the IH model base grid of ∼1°.4 × 1°.4. We also scale the WSA magnetic field strengths by a factor of 3 during this process to compensate for the systematic underestimation of the open magnetic flux at 1 au (Linker et al. 2016, 2017; Wallace et al. 2019). This factor has been selected to improve the match of observations and simulations at Earth. We have used the same factor in Singh et al. (2020). We estimate the radial and azimuthal components of the magnetic field at 0.1 au from the WSA B values using the local SW speed to account for the Sun's rotation because the SW propagates radially outward from 1 $R_\odot$ to 0.1 au (MacNeice et al. 2011). We reduce the WSA speeds by 20% to account for the difference in SW acceleration between the WSA and MS-FLUKSS models (e.g., MacNeice et al. 2011; Kim et al. 2014). Kim et al. (2014) showed that using this reduction factor results in an improved matching of observed and simulated parameters at Earth. To estimate the SW density and temperature at 0.1 au, we use the empirical correlations

between the SW speed, density, and temperature based on OMNI data (Elliott et al. 2016). These procedures give us all inner boundary conditions required to simulate SW in the IH.

2.2.2. CME Model

In this work, to simulate flux-rope-based CMEs, we use the geometry of the FRiED model (Isavnin 2016) and describe the initial magnetic field in it in accordance with the uniform-twist analytic solution described by Vandas & Romashets (2017). The geometry of the FRiED model simplifies the CME shape to a croissant-like structure with two legs rooted at the center of the Sun, as shown in the left panel of Figure 2. This geometry is characterized by the parameters R_t, R_p, and $\phi_{\rm hw}$, as shown in the figure. The flux rope has a circular cross section with a curved axis shown by the dashed black line. The radius of this cross section, $R(\phi)$, is specified using the formula

$$R(\phi) = \frac{R_p}{R_t}r(\phi), \qquad (1)$$

where $r(\phi)$ is the distance of the curved axis from the origin. This distance is defined by the formula

$$r(\phi) = R_t \cos^n\left(\frac{\pi}{2}\frac{\phi}{\phi_{\rm hw}}\right), \qquad (2)$$

where n is a free parameter that can be used to adjust the flatness of the flux rope shape.

We found that the flux rope geometry of the FRiED model can be matched very well with the GCS model, designed with any suitable choice of its parameters, by appropriately selecting the FRiED parameters. For example, the outer boundary of a GCS-shaped flux rope with half-width $\rm hw_{GCS} = 33°$, height $H_{\rm GCS} = 70\,R_\odot$, and aspect ratio $\kappa = 0.5$ matches very well with the FRiED flux rope with $R_t = 46.67\,R_\odot$, $R_p = 23.33\,R_\odot$, half-width $\phi_{\rm hw} = 40°$, and $n = 0.33$, as shown in the right panel of
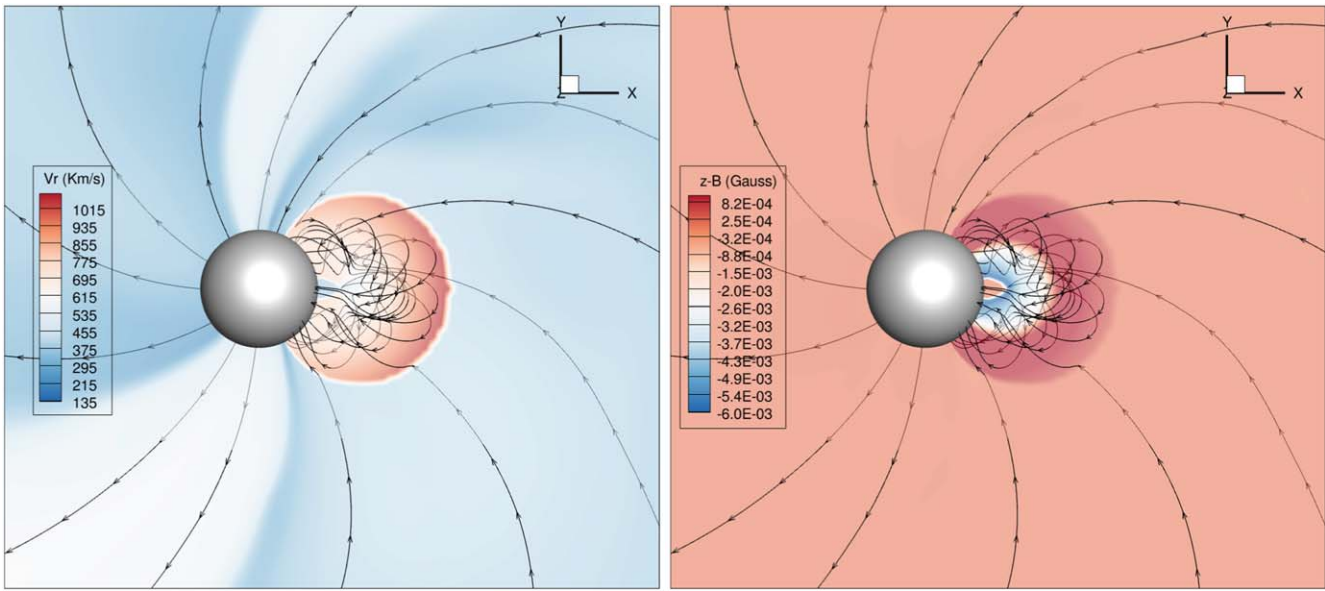
Figure 3. The initial structure of the constant-turn flux rope model with the apex speed of 1100 km s^{-1}, poloidal flux of 1.4×10^{22} Mx, and toroidal flux of 7.6×10^{21} Mx when inserted into the IH. The apex of the flux rope is at 70 $R_\odot$, while its latitude, longitude, and tilt are zero. The $z = 0$ semitranslucent slices of radial velocity (left panel) and B_z (right panel) are shown along with the magnetic field lines. The gray sphere represents the inner boundary of the IH model at 0.1 au.

Figure 2. The choice of parameters for these shapes is suitable for the 2012 July 12 CME, which we are going to study below.

We use the uniform-twist solution of Vandas & Romashets (2017) because some recent studies (e.g., Hu et al. 2015) show that in situ signatures of the ICME magnetic field are consistent with a constant-turn configuration. Since the FRiED model has a curved geometry, we cannot use constant-turn cylindrical flux rope models such as the Gold–Hoyle model (Gold & Hoyle 1960) to describe the magnetic field in it. However, a magnetic field solution in a curved shape such as a torus is more compatible with FRiED model geometry. Vandas & Romashets (2017) give the analytic solution of a constant-turn magnetic field in a torus shape as

$$B_r = 0; \quad B_\phi = \frac{B_0}{1 + b^2 r^2};$$
$$B_\theta = -\frac{B_0 R_0 b r}{(1 + b^2 r^2)(R_0 + r \cos\theta)}. \tag{3}$$

Here r, θ, and ϕ are the coordinates of the toroidally curved cylindrical system, which is described in detail in Section 2 of Vandas & Romashets (2017). The parameters B_0 and b control the magnetic flux and the number of magnetic field line turns, respectively. R_0 is the major radius of the torus. Since the FRiED geometry is not exactly a torus, we define the magnetic field distribution in the structure by assuming it to be locally toroidal. The parameter B_0 is modified inside the flux rope to conserve the inserted axial (toroidal) flux. The value of b can be estimated from the inserted poloidal flux inside the flux rope. We fix R_0 throughout the flux rope so that the introduced positive and negative poloidal fluxes are within 20% of each other. This means that the magnetic flux directed into the plane containing the curved axis of the flux rope is within 20% of the magnetic flux directed out of this plane.

In this model, we define the initial velocity at any location inside the flux rope as a combination of the radial and expansion velocities, i.e., $V = V_{\text{rad}} + V_{\text{exp}}$, where V_{rad} is in the radial direction away from the origin (the Sun's center) and V_{exp} is in the direction pointing away from the curved axis. The speed at the apex is considered to be the CME speed V_{CME}. To

facilitate a self-similar expansion, we specify

$$|V_{\text{rad}}| = \frac{V_{\text{CME}}}{1 + R_p/R_t}, \quad |V_{\text{exp}}(r_p)| = \frac{r_p}{R_t}|V_{\text{rad}}|,$$

where r_p is the radial coordinate inside the local torus structure. This specification can be readily derived from the self-similar properties $R_p \propto R_t$ and $r_p \propto R(\phi)$. Initially, we assume a constant density inside the flux rope.

We insert this flux rope into the ambient SW in such a way that the flux rope is initially superimposed with the SW background. This superimposition is described in detail in Singh et al. (2020). It should be noted that this approach is different from the other, more commonly used approach, where a flux rope is inserted at the inner boundary gradually (e.g., Shiota & Kataoka 2016; Verbeke et al. 2019). Our method of flux rope insertion into the SW preserves the CME flux rope much more accurately, exhibiting a curved front and two legs. On the other hand, the gradual, step-by-step insertion of flux ropes at the inner boundary can be problematic because of their unnatural initial expansion, which must then be compensated by introducing the flux rope with initial speeds smaller than observed. We introduce the flux rope parameters as follows:

1. $\mathbf{B}_{\text{final}} = \mathbf{B}_{\text{FR}}$,
2. $\rho_{\text{final}} = \rho_{\text{FR}} + \rho_{\text{SW}}$,
3. $e_{\text{final}} = e_{\text{FR}} + e_{\text{SW}}$.

Here $\vec{B}_{\text{FR}}$ is given by Equation (3), ρ is the plasma density, and e is the total energy density. We also note that

$$e_{\text{FR}} = \frac{|\mathbf{B}_{\text{FR}}|^2}{8\pi}, \quad e_{\text{SW}} = \frac{p_{\text{SW}}}{\gamma - 1} + \frac{|\mathbf{B}_{\text{SW}}|^2}{8\pi} + \frac{\rho_{\text{SW}}|\mathbf{v}_{\text{SW}}|^2}{2},$$

where p and $\mathbf{v}$ are the thermal pressure and bulk velocity, respectively. We have kept the adiabatic index $\gamma = 1.5$ in this study.

In Figure 3, we show an example of such an insertion. The flux rope has the following FRiED parameters: $R_t = 46.67$, $R_p = 23.33$, $\phi_{\text{hw}} = 40°$, and $n = 0.33$. The flux rope is assigned
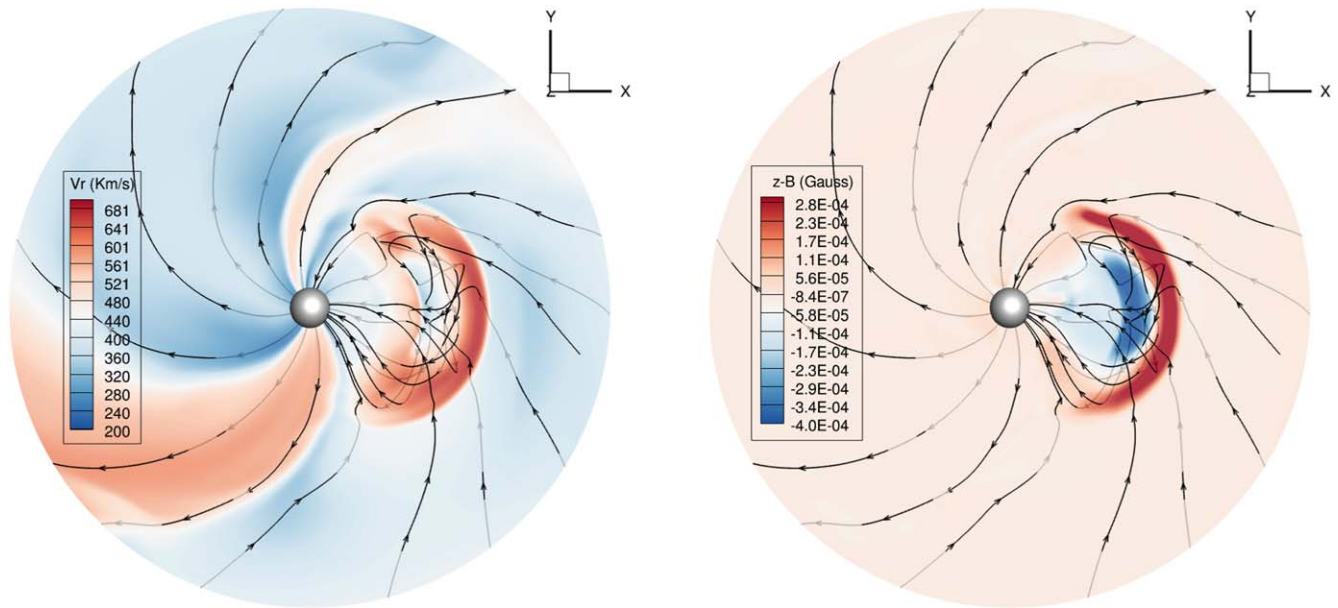
Figure 4. The flux rope shown in Figure 3 30 hr after the initial insertion is propagating as an ICME. The $z = 0$ semitranslucent slices of radial velocity (left panel) and B_z (right panel) are shown along with the magnetic field lines. The gray sphere represents the inner boundary of the IH model at 0.1 au.

an initial speed of 1100 km s^{-1}, a poloidal flux of 1.4×10^{22} Mx, and a toroidal flux of 7.6×10^{21} Mx. It is initialized with zero latitude, longitude, and tilt. The helicity sign is kept positive. A flux rope with these properties is chosen because we will later simulate the 2012 July 12 CME with the same parameters. The left panel of Figure 3 shows the velocity distribution in the $z = 0$ slice of this flux rope, along with the magnetic field lines inside it. The right panel of Figure 3 shows the distribution of B_z in the $z = 0$ plane. The gray sphere represents the inner boundary of our simulation domain at 0.1 au. The SW background shown here is on 2012 July 12 at 21:30 UT.

After the initial insertion, the model flux rope propagates through the IH as an ICME. In Figure 4, we show the model ICME after 30 hr of propagation. The apex speed of the ICME has dropped to about 700 km s^{-1} by this time, and the B_z values have also reduced owing to the ICME expansion. This example shows that our model can be used to simulate ICMEs in the IH.

3. Results

3.1. 2012 July 12 CME

In this section, we present the simulation results for the 2012 July 12 CME. We have found the linear speed, latitude, longitude, tilt, half-angle, and aspect ratio of this CME to be 1265 km s^{-1}, $-10°$, $1°$, $52°$, $33°$, and 0.5, respectively, at $15 R_\odot$. Since we introduce our model CME into the SW background in a single step, we have to introduce the CME when its apex has already reached a height of $70 R_\odot$, as we show in Figure 3. We assumed a self-similar CME expansion from 15 to $70 R_\odot$ to propagate the model CME from 15 to $70 R_\odot$. Using the DBM (Vršnak & Zic 2007), we estimated that the CME should reach the apex height of $70 R_\odot$ on 2012 July 13 03:33 with a speed of about 1097 km s^{-1}. We used the drag parameter of 0.1×10^{-7} and the asymptotic SW speed equal to 450 km s^{-1} here. Vršnak et al. (2014) found that this combination of drag parameters ensures roughly the same

arrival time accuracy for the DBM and WSA-ENLIL-Cone models. We also found that the poloidal flux carried by this CME is 1.4×10^{22} Mx. This value is found from the reconnected flux under the PEA of the source AR using the method described by Gopalswamy et al. (2018b). We used this value in the empirical relation between the ICME poloidal and toroidal fluxes (Qiu et al. 2007) to calculate the toroidal flux of this CME to be 7.6×10^{21} Mx. The helicity sign of this CME was found to be positive (Singh et al. 2019). Using the CME brightness in the coronagraph images, we found that the CME mass is 1.65×10^{16} g. The brightness is due to the Thomson scattering of photospheric light by the plasma electrons (Billings 1966). By integrating over the CME area and removing the projection effects with the help of multiple coronagraph images, we can calculate the true mass of the CME (Colaninno & Vourlidas 2009), which includes the contribution from the CME sheath, cavity, and core. However, we insert only the flux rope part of a CME into the ambient SW, which resides in the cavity region and has a density much lower than the sheath and core densities (Riley et al. 2008). Therefore, we added only 1.65×10^{13} g of uniformly distributed extra mass inside the model flux rope to the ambient (background) SW. As shown below, introducing this fraction of the total mass ensures a reasonable agreement with the observed ICME density at Earth. However, it needs to be investigated further if this fraction of total mass is appropriate for other CMEs.

Figure 5 shows our comparison between the observations and simulations at Earth. We use the 1 hr averaged SW data provided by NASA/GSFC through OMNIWeb (King & Papitashvili 2005). Visual inspection shows that the ICME arrives at Earth with a turbulent sheath, followed by a magnetic cloud with a smoothly rotating magnetic field. The distribution of magnetic field in the cloud has peaks in the negative direction for all RTN components. Please note that by peaks we mean maximum excursion, and this definition is valid for the rest of the paper. Comparing our simulation results to observations, we find that there is a reasonable agreement in
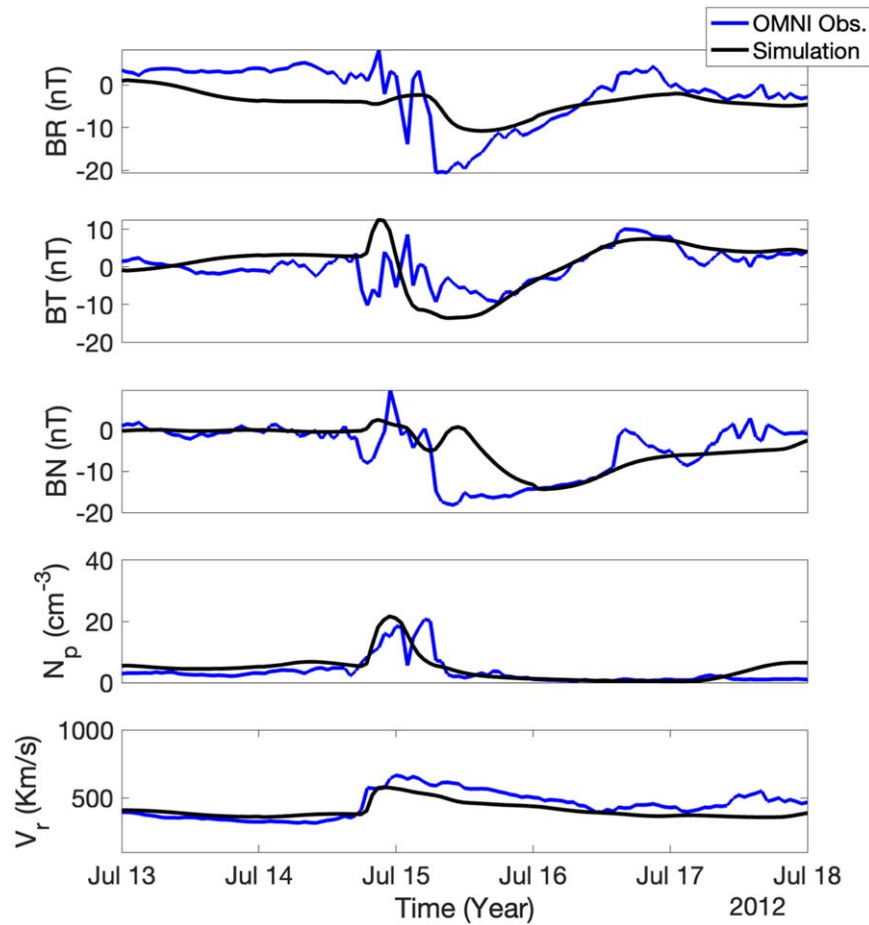
Figure 5. Comparison of the 1 hr averaged OMNI SW data (blue) and simulation results at Earth (black). The simulated ICME arrived 1 hr after the observed ICME. The signs of the peaks in the magnetic field distribution inside the ICME cloud agree well for all three components. The N-component of any vector in the RTN coordinate system is comparable to the z-component in the GSE coordinate system.

the density, speed, and magnetic field values. Our simulations were able to reproduce the signs of the peaks in all three components of the magnetic field inside the ICME cloud. The peak values of the RTN components of the magnetic field inside the observed cloud were $(-12, -9, -18)$ nT. The corresponding values in the simulated ICME cloud were $(-11, -14, -14)$ nT. This agreement in the magnetic field seems to be better than in the previously reported simulation studies of the same CME (Shen et al. 2014; Scolini et al. 2019; Singh et al. 2020). The simulated ICME arrived just 1 hr behind the observed ICME. The simulated density, in both the sheath region and the magnetic cloud, matches well with the observations, although we inserted only 0.1% of the observed mass in the initial flux rope. However, we do notice that the density in the sheath region is much smoother in our simulation as compared to the observation. We also note that the simulated speed at the ICME front agrees with observations. Inside the ICME, our simulation shows speeds moderately lower than in the observations. Worth noticing are some differences between the model background SW and OMNI data ahead of the interplanetary shock arrival on 2012 July 14, which can be a possible source of errors in the sheath region. First, the background magnetic field polarity is different in the modeled and observed SW, which contributes to the errors in the simulated sheath magnetic field. Second, the model SW is slightly denser and faster than observed.

In our previous study, we simulated this CME using the modified spheromak model (Singh et al. 2020), which did not reproduce the negative value of B_r. In future studies, we will compare the modified spheromak and constant-turn models in more depth to determine whether the constant-turn model performs consistently better than the modified spheromak model. This ICME had been modeled previously by Shen et al. (2014) and Scolini et al. (2019) with the magnetized plasma blob and spheromak models, respectively. The magnetic field components obtained with our constant-turn model seem to agree with observations much better than in the above-mentioned studies.

The kinematic and magnetic properties of CMEs derived from observations contain some level of uncertainty. In the next subsections, we will address the uncertainties associated with GCS fittings and analyze their effects on the CME simulation results at Earth. We only focus on the uncertainties due to GCS fitting. The impact of the uncertainties in the magnetic field flux estimates on the CME properties at Earth will be considered elsewhere.

3.2. GCS Uncertainty Analysis

The GCS model is a useful tool to derive the 3D properties of CMEs using multiple viewpoint images. However, the derived properties can have large uncertainties, due to the idealization of the CME shape to be a symmetrical, two-conical-leg structure

with a curved front that is propagating radially outward. In reality, CMEs can be highly asymmetrical, skewed, and/or slanted with respect to the radial direction. Moreover, SOHO and STEREO-A/B roughly belong to the same ecliptic plane. The direction of the CME out of this ecliptic plane is roughly its latitude value, and it can be easily fitted with the GCS model because all three viewpoints will show a similar extent of the CME out of this plane. The direction of the CME in the ecliptic plane is roughly its longitude value. Estimating this direction with the GCS model is challenging compared to estimating the latitude because all three viewpoints will show different extents of the CME in this direction. This means that GCS fitting based on SOHO and STEREO data can result in larger ambiguities in the longitude estimates as compared to latitude estimates.

Apparently, the estimates of GCS parameters can vary depending on the fitting approach. Here we try to estimate the average subjective uncertainties for the same CMEs when fitted by different GCS users. Using GCS fitting results reported in different publications, as well as in online catalogs, we compiled six lists of CMEs. For example, Gopalswamy et al. (2014) fitted 77 CMEs that had erupted between 2010 February and 2014 January and reported their latitudes, longitudes, and speeds. Thernisien et al. (2009) reported the latitudes, longitudes, tilts, and half-angles of 26 CMEs that erupted between 2007 November and 2008 August. Shi et al. (2015) reported latitudes, longitudes, and speeds of 21 CMEs that erupted between 2008 December and 2012 October. CME Kinematic Database (KINCAT; Millward et al. 2013) reports GCS latitudes, longitudes, tilts, speeds, half-angles, and aspect ratios of 122 CMEs that erupted between 2007 May and 2013 October. The full halo CME (FHCME) catalog (Shen et al. 2013) has GCS fitting results for the latitudes, longitudes, and speeds of 39 front-side halo CMEs between 2009 December and 2012 May. Finally, we also used our own unpublished catalog of GCS fittings for 49 CMEs that erupted between 2010 February and July 2012. All these GCS fittings apply linear regression to the height−time data to obtain CME speed.

Using the above-mentioned CME lists, we identified the CMEs that appeared in at least two of the lists and published the GCS parameters of those CMEs (see https://doi.org/10.5281/zenodo.5515483), which allowed us to compare the estimated latitude and longitude values of 56 CMEs, tilt values of 22 CMEs, and speed values of 18 CMEs. We define the subjective uncertainty in a GCS parameter for a CME as the range of measurements i.e., difference between maximum and minimum values of this parameter reported in the lists that contained the same CME. For example, if a CME appeared in three of the lists that had the latitude estimates of $1°$, $5°$, and $10°$, the subjective uncertainty in latitude for that CME would be $9°$. The speed uncertainty can be better represented by the speed fractional uncertainty because speed uncertainty itself can be higher for faster CMEs than for slower ones. The speed fractional uncertainty can be specified as

$$\text{Speed Fractional Uncertainty} = \frac{\text{Speed Uncertainty}}{\text{Average Speed in Separate Fits}}.$$

The distributions of subjective uncertainties for GCS estimates of the considered CMEs are shown in Figure 6. We further found the average of these uncertainties. We found that the GCS estimates of latitude, longitude, and tilt show an average uncertainty of $5°.7$, $11°.2$, and $24°.7$, respectively. We can see that the latitude uncertainties are significantly smaller than the longitude uncertainties, which is because the observing

spacecraft are all roughly in the ecliptic plane. The tilt uncertainties are much higher than the latitude and longitude uncertainties. We can see that 4 of the 22 CMEs had tilt uncertainties of more than $40°$. We also found that, on average, CMEs can have uncertainties in their speed of about 11.4%.

Thernisien et al. (2009) used the sensitivity analysis to estimate the average uncertainties in GCS parameters of 26 CMEs they considered in their study. They found the average uncertainties in latitude, longitude, and tilt to be $1°.8$, $4°.3$, and $22°$, respectively, which are smaller than the values we found by comparing the fittings provided by different users of the GCS model. The difference in these values is due to the choice of CMEs used in the studies and/or due to the different methods of finding these uncertainties. Thernisien et al. (2009) used a theoretical approach to estimate the uncertainties, whereas we used a practical approach in which we directly compared the fitting results of different users of the GCS model. The average uncertainties in the CME tilt in Thernisien et al. (2009) and in our analysis are comparable.

3.3. Ensemble Modeling

Pizzo et al. (2015) showed that MHD modeling of CMEs does not depend on the changes in their initial properties chaotically. This means that ensemble modeling of CMEs can be performed to get estimates of the CME forecast uncertainties by creating ensemble members according to the uncertainties in the initial CME model parameters. To study the propagation of uncertainties in the GCS parameters to the CME forecasting uncertainties, we have performed an ensemble modeling for the 2012 July 12 CME using our constant-turn model. We created the ensemble members by taking into consideration the average uncertainties in latitude, longitude, tilt, and speed. Out of the five external lists of reported GCS parameters considered in our study, only the KINCAT database reports half-angles and aspect ratios. Therefore, we could not find the average uncertainties of aspect ratio and half-angle by comparing them across the lists. Instead, we used the uncertainty values reported in Thernisien et al. (2009). They were $+ 0.07 / − 0.04$ and $+ 13°/ − 7°$ for the aspect ratios and half-angles, respectively.

We created 77 ensemble members for our CME. These members are described by different GCS parameters used to initiate the CME model. The first member is the one with our own estimated values of the 2012 July 12 CME parameters. An ensemble member with the GCS properties of latitude θ, longitude ϕ, tilt γ, speed V_{CME}, half-angle α, and aspect ratio κ can be represented by a set $\{\theta, \phi, \gamma, V_{\text{CME}}, \alpha, \kappa\}$. The other 76 ensemble members can be represented by the following sets:

1. $\{\theta \pm 5°.7, \phi \pm 11°.2, \gamma \pm 24°.7, V_{\text{CME}} \pm 11.4\%, \alpha_{-7°}^{+13°}, \kappa_{-0.04}^{+0.07}\}$ (64 members)
2. $\{\theta \pm 5°.7, \phi, \gamma, V_{\text{CME}}, \alpha, \kappa\}$ (2 members)
3. $\{\theta, \phi \pm 11°.2, \gamma, V_{\text{CME}}, \alpha, \kappa\}$ (2 members)
4. $\{\theta, \phi, \gamma \pm 24°.7, V_{\text{CME}}, \alpha, \kappa\}$ (2 members)
5. $\{\theta, \phi, \gamma, V_{\text{CME}} \pm 11.4\%, \alpha, \kappa\}$ (2 members)
6. $\{\theta, \phi, \gamma, V_{\text{CME}}, \alpha_{-7°}^{+13°}, \kappa\}$ (2 members)
7. $\{\theta, \phi, \gamma, V_{\text{CME}}, \alpha, \kappa_{-0.04}^{+0.07}\}$ (2 members)

The 64 members in set 1 represent all possible combinations of GCS parameter extremes, where the GCS parameters we estimated for the 2012 July 12 CME differ according to the average uncertainties in these parameters. The simulation of
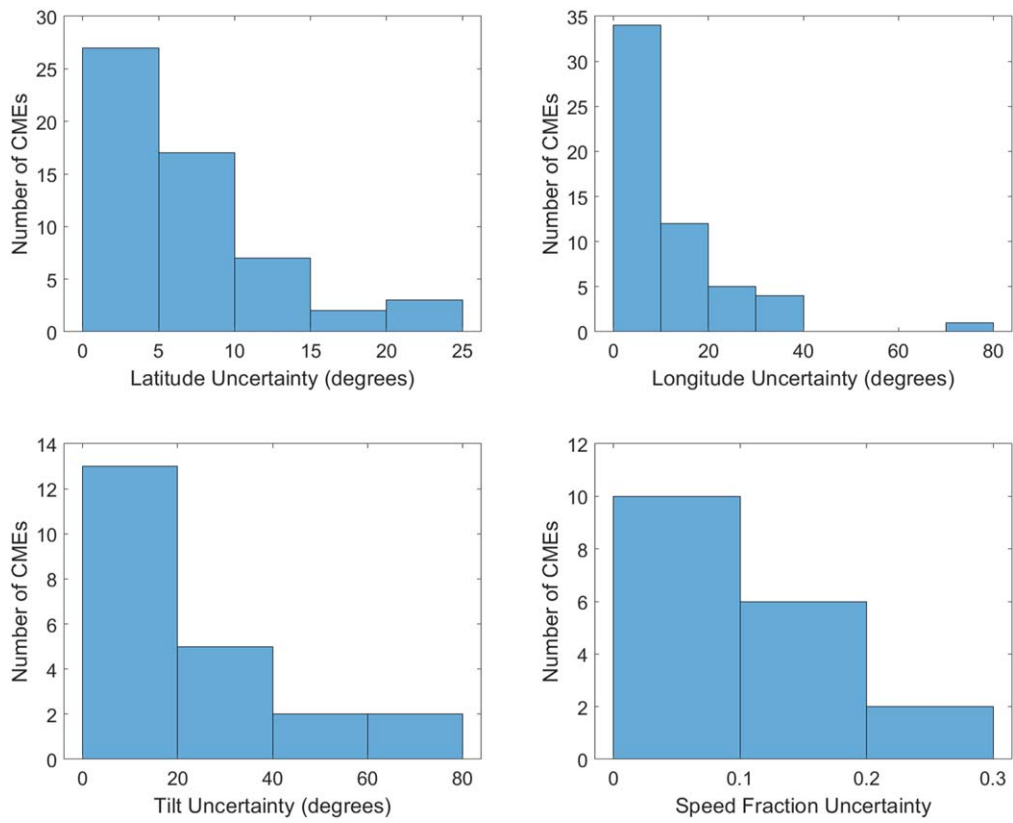
Figure 6. Histograms showing the distribution of uncertainties in GCS estimates of latitude (top left), longitude (top right), tilt (bottom left), and speed fraction (bottom right).
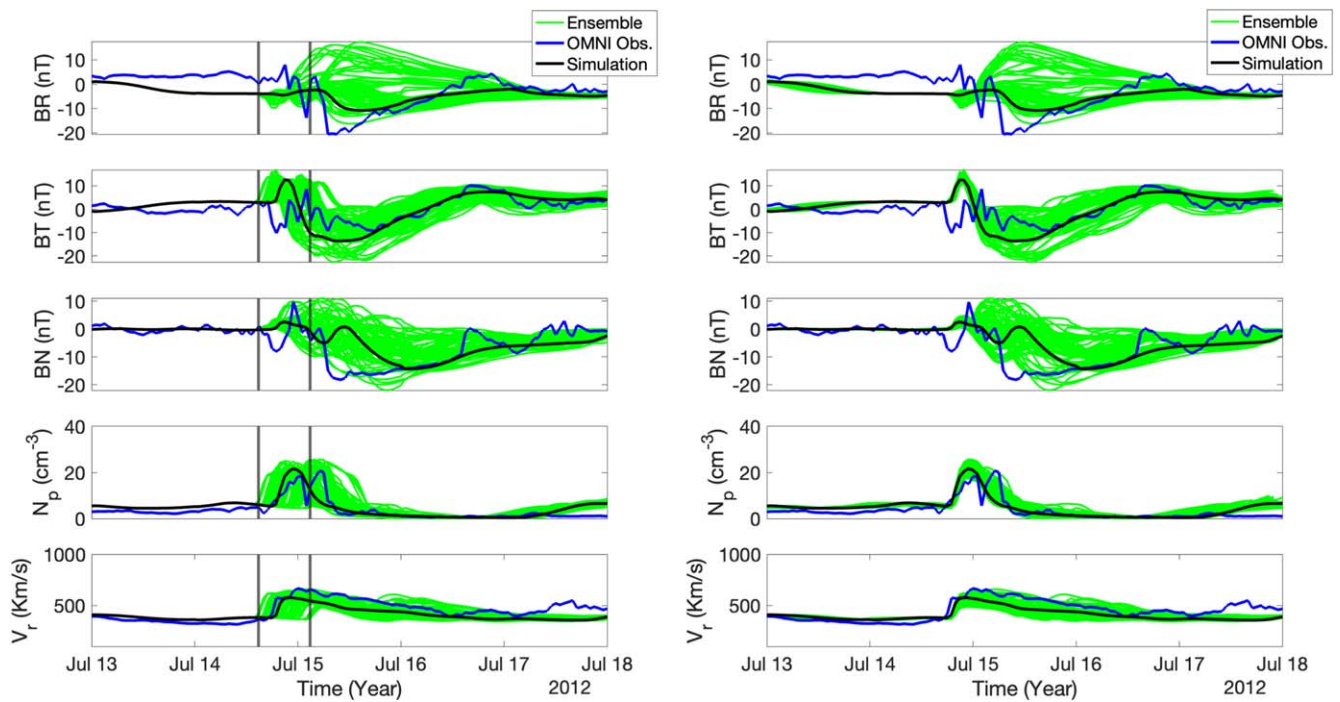

Figure 7. Left panel: plasma and magnetic field in the 1 hr averaged OMNI SW data (blue) and simulation results probed at Earth (black and green). The black line represents the first ensemble member with GCS parameters found by us. The green lines represent the rest of the 76 ensemble members defined in Section 3.3. The gray vertical lines show the 12 hr wide arrival time window of all the ensemble members. Right panel: same as the left panel, but with the arrival time of all ensemble members matched with the first member.
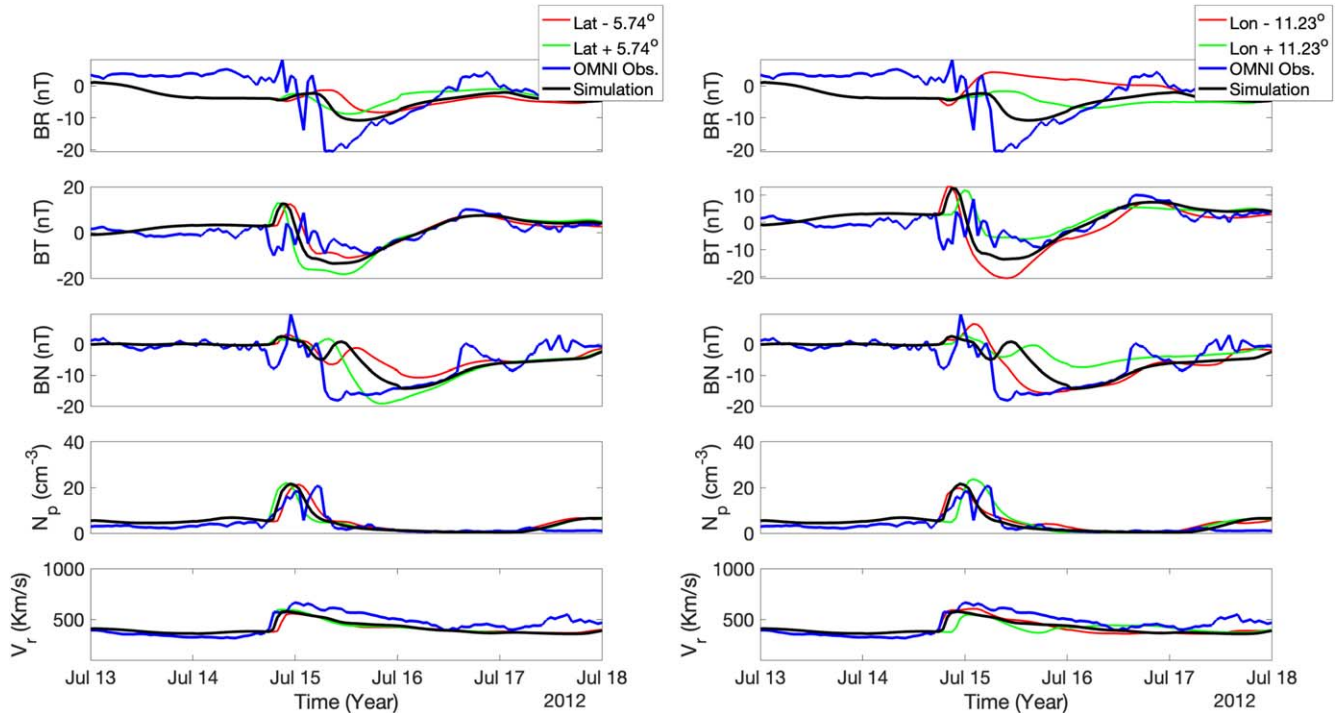
Figure 8. The distributions of plasma velocity and density, and magnetic field components in the 1 hr averaged OMNI data (blue) and simulation results at Earth (black, red, and green). The black lines represent the first ensemble member with our derived GCS parameters. The red and green lines represent the two ensemble members defined in sets 2 (left panel) and 3 (right panel) in Section 3.3.

these ensemble members should give us the upper and lower bounds of simulation uncertainties due to subjective uncertainties in the GCS fitting. The 12 members in sets 2–7 are used in this work to study the individual contribution of uncertainties in each parameter to the simulation results at Earth.

In the left panel of Figure 7, we compare all ensemble members with OMNI data at Earth. The members show a 12 hr wide arrival window bounded by gray vertical lines. The peak speed at the time of arrival ranges between 480 and 610 km s^{-1}. The peak density of the front of ICMEs ranges between 18 and 26 cm^{-3}. In the right panel of Figure 7, we show the ensemble members by shifting them in time to match the individual arrival times to that of the first ensemble member. This is done for an easier qualitative comparison of the plasma and magnetic field values in the ensemble members. While 55% of the ensemble members correctly reproduced the peak signs for all three components of the cloud magnetic field, a significant fraction did not correctly reproduce the sign of the peak in the radial magnetic field component.

To investigate the effects of uncertainty in each GCS parameter on the simulation results, we used sets 2–7, where each of the GCS parameters was modified according to its average uncertainties, keeping the rest of the parameters unchanged. This exercise provides a rather good insight into the role of uncertainties in the individual GCS parameters in producing the CME model uncertainties at Earth.

The left panel of Figure 8 shows the effect of uncertainties in latitude on CME forecasting at Earth. The latitude uncertainty of $\pm 5°.74$ widens the arrival time window by 2 hr. This uncertainty, however, does not change the signs of the peaks in the cloud magnetic field components, which all remain negative. As mentioned in Section 3.1, the peak RTN components of the ICME magnetic cloud of our simulated

CME were $(-11, -14, -14)$ nT. By varying the latitude by $\pm 5°.74$, we obtain the peak values of the RTN components equal to $(-9, -18, -19)$ and $(-8, -11, -11)$ nT.

The effect of the longitude uncertainty on magnetic field forecasts in the cloud is much more pronounced, as can be seen in the right panel of Figure 8. The longitude uncertainty of $\pm 11°.23$ gives the range of the peaks in the RTN components equal to $(-7, -7, -7)$ nT and $(4, -20, -16)$ nT. We can see that a $-11°.23$ change in latitude results in the wrong sign of B_r. Besides, a $\pm 11°.23$ uncertainty in longitude widens the arrival time window by 3 hr.

The tilt uncertainty of $\pm 24°.71$ can significantly alter the magnetic field profile in the magnetic cloud of ICME at Earth, as shown in the left panel of Figure 9. Such tilt range can change the peak values of the RTN components of the cloud magnetic field from $(-11, -14, -14)$ nT to $(-5, -17, -20)$ nT or $(-8, -10, -10)$ nT. The tilt uncertainty, however, does not change the signs of the peak magnetic field components from being negative. The arrival time window is widened by 1 hr owing to the tilt uncertainty.

In the right panel of Figure 9, we show the effect of a $\pm 11.4\%$ uncertainty in speed on the simulated signatures of ICMEs at Earth. One can see that the speed uncertainty does not change the magnetic field profile in the ICME cloud. This uncertainty, however, widens the arrival time window by 6 hr. We also found that the peak density stays unaffected by the ICME speed change. This result is in line with the recent observational analysis by Temmer et al. (2021). It should also be noted that the arrival time window with the full set of ensemble members had a width of 12 hr. This shows that the arrival time window can be widened by as much as 100% by the combination of uncertainties in CME parameters, as compared to uncertainties in initial speed only.
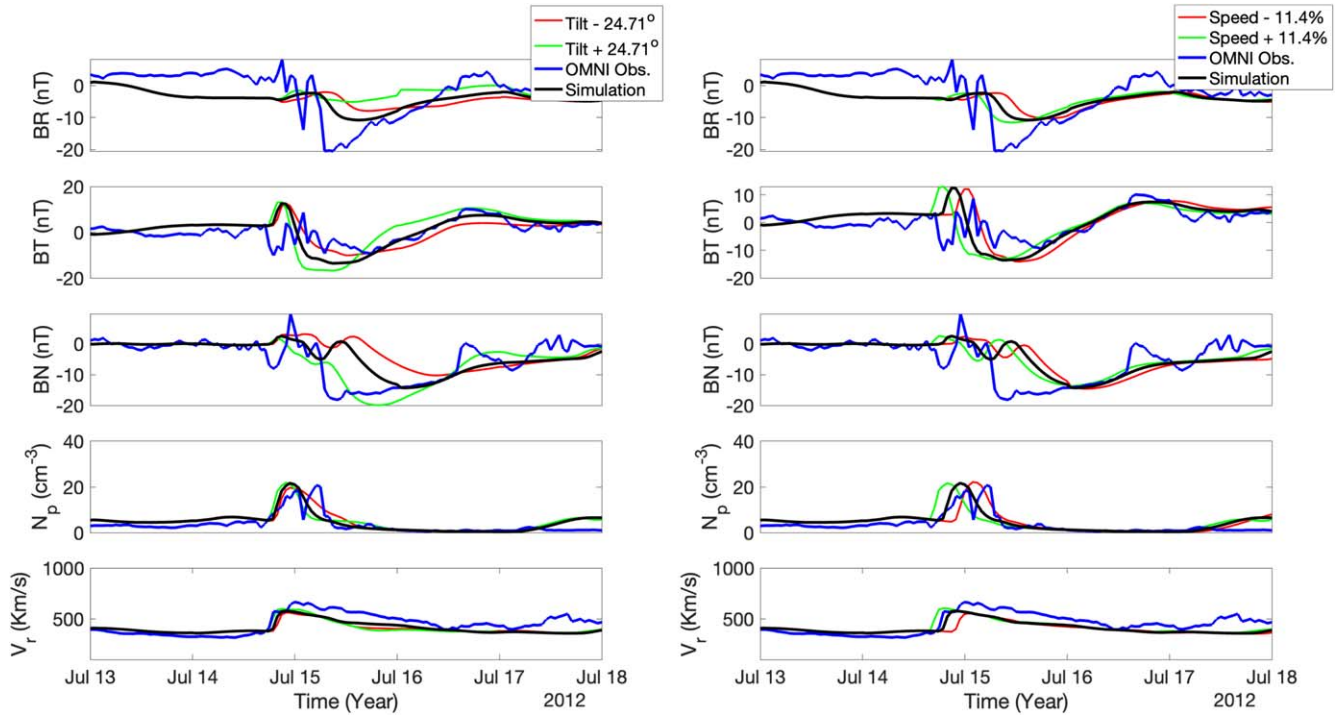
Figure 9. Plasma speed and density, and magnetic field component distributions in the 1 hr averaged OMNI SW data (blue) and simulation results at Earth (black, red, and green). The black line represents the first ensemble member with our derived GCS parameters. The red and green lines represent the two ensemble members defined in sets 4 (left panel) and 5 (right panel) in Section 3.3.
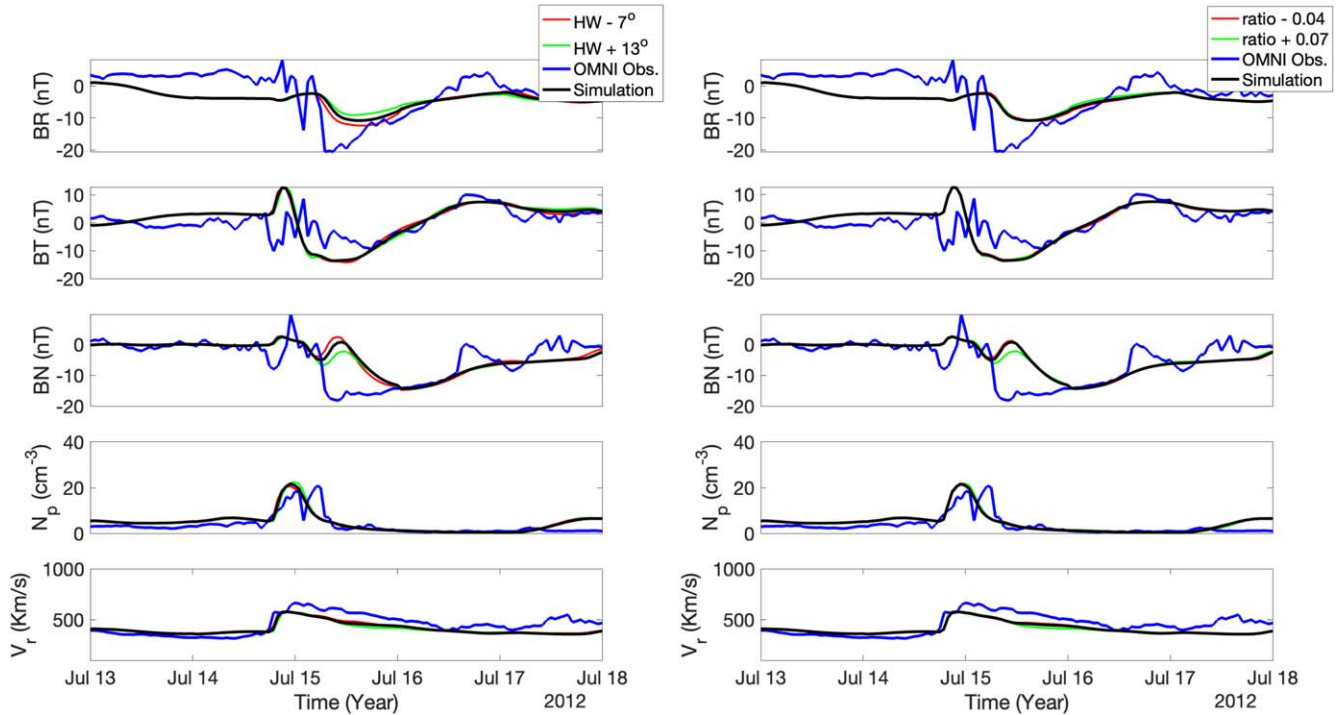

Figure 10. Plasma speed and density, and magnetic field components in the 1 hr averaged OMNI SW data (blue) and simulation results at Earth (black, red, and green). The black line represents the first ensemble member with our derived GCS parameters. The red and green lines represent the two ensemble members defined in sets 6 (left panel) and 7 (right panel) in Section 3.3.

Figure 10 shows the effect of $+13°/-7°$ half-width $+0.07/-0.04$ aspect ratio uncertainties (the left and right panels, respectively). Both of these uncertainties result in very small changes in the magnetic field and plasma properties at Earth. The arrival time is also largely unaffected by these

uncertainties. The ensemble member with the larger half-width has a slightly larger density peak of the front (by 2 cm^{-3}), which might be due to a larger mass pileup at the front during its interplanetary travel. This has been shown also in the observations of Temmer et al. (2021), which show that wider

ICMEs tend to have stronger mass pileup at the front. Since the 2012 July 12 CME was Earth directed, we did not expect the half-width to play a major role in controlling the 1 au signature of this ICME. However, off the Sun−Earth line CMEs can be affected by the uncertainties in half-width to a larger extent. This is because such uncertainties can create an ICME with magnetic clouds either passing over Earth or missing it.

4. Conclusion

In this study, we have implemented a flux rope model with a constant-turn magnetic field (Vandas & Romashets 2017) to perform MHD simulations of the 2012 July 12 CME propagation through a time-dependent, data-driven ambient SW. The CME shape used in our model is based on the FRiED approach described by Isavnin (2016). It can be matched well with the shape approximation used in the GCS model, which is frequently used to derive 3D properties of CMEs from the analysis of multiviewpoint images made by coronagraphs. We constrain the poloidal magnetic flux in this model with the measured reconnected flux in the PEAs of the source AR. The toroidal magnetic flux is estimated from the poloidal flux using the empirical relation given by Qiu et al. (2007). We have shown that by constraining the flux rope model with GCS and PEA observations of the 2012 July 12 CME, the ICME features at Earth are reproduced with reasonable accuracy. Our simulated CME agrees with the observations of speed, density, and the signs of the magnetic field components in the ICME magnetic cloud. The arrival time of our simulated ICME was off by just 1 hr.

We compared the GCS parameters calculated independently by multiple users to derive the average subjective uncertainties in the CME latitude, longitude, tilt, and speed, which turned out to be $5°74$, $11°23$, $24°71$, and 11.4%, respectively. Using these uncertainties, as well as those in the CME half-angle and aspect ratio $(+13°/-7°$ and $+0.07/-0.04$, respectively) from Thernisien et al. (2009), we have created 77 ensemble members for the 2012 July 12 CME. The results of our ensemble modeling are summarized as follows:

1. The arrival time window for the full ensemble is 12 hr wide. This value is similar to the typical arrival time errors obtained with different models. This 12 hr width of the full ensemble is due to the combined nonlinear impact of uncertainties in all GCS model parameters.

2. A total of 55% of the ensemble members correctly reproduced the signs of all RTN components of the peak magnetic field in the ICME magnetic cloud, while 28% of the ensemble members did not produce the correct sign of B_r.

3. Subjective uncertainties of $\pm 11°23$ in longitude and $\pm 24°71$ in the CME tilt are found to be the main sources of uncertainty in the simulated magnetic field. Subjective uncertainty of $\pm 5°74$ in latitude had a lesser impact on the simulated magnetic field values. This highlights the importance of out-of-ecliptic coronagraph observations of CMEs, which would be very important for better constraining the CME longitude.

4. Uncertainties in the half-width and the aspect ratio are hardly affecting the ICME features at 1 au. This is not surprising, since our CME was Earth directed. The half-angle of a model CME may play an important role for the CMEs that are not aligned with the Sun−Earth line.

It takes about 2 hr of computation for MS-FLUKSS to simulate about 6 days of physical time on a $150 \times 128 \times 256$ grid using 128 CPUs. Since we can run all ensemble members in parallel, the ensemble modeling we have performed here is feasible for real-time space weather forecasting. It is of importance to note that we have not considered the uncertainties in the input magnetic fluxes. Incorporating those uncertainties into the analysis may significantly increase our ensemble size. However, since the half-width and aspect ratio of the CME were shown to have minimal effect on the simulation results at Earth, we could still create ensembles of reasonable size by excluding those members.

ORCID iDs

Talwinder Singh ⊙ https://orcid.org/0000-0002-0213-6038
Tae K. Kim ⊙ https://orcid.org/0000-0003-0764-9569
Nikolai V. Pogorelov ⊙ https://orcid.org/0000-0002-6409-2392

References

Amari, T., Canou, A., & Aly, J.-J. 2014, Natur, 514, 465
Amerstorfer, T., Hinterreiter, J., Reiss, M. A., et al. 2021, SpWea, 19, e02553
Amerstorfer, T., Möstl, C., Hess, P., et al. 2018, SpWea, 16, 784
Arge, C. N., de Toma, G., & Luhmann, J. G. 2005, in ASP Conf. Ser. 346, Large-scale Structures and their Role in Solar Activity, ed. M. Penn & A. Pevtsov (San Francisco, CA: ASP), 371
Arge, C. N., Henney, C. J., Hernandez, I. G., et al. 2013, in AIP Conf. Proc. 1539, Solar Wind 13 (Melville, NY: AIP), 11
Arge, C. N., Henney, C. J., Koller, J., et al. 2010, in AIP Conf. Proc. 1216, Twelfth Int. Solar Wind Conf. (Melville, NY: AIP), 343
Arge, C. N., Henney, C. J., Koller, J., et al. 2011, in ASP Conf. Ser. 444, V International Conference of Numerical Modeling of Space Plasma Flows (ASTRONUM 2010), ed. N. V. Pogorelov, E. Audit, & G. P. Zank (San Francisco, CA: ASP), 99
Arge, C. N., Odstrcil, D., Pizzo, V. J., & Mayer, L. R. 2003, in AIP Conf. Proc. 679, Solar Wind 10 (Melville, NY: AIP), 190
Billings, D. E. 1966, A Guide To The Solar Corona (New York: Academic Press)
Brueckner, G. E., Delaboudiniere, J.-P., Howard, R. A., et al. 1998, GeoRL, 25, 3019
Brueckner, G. E., Howard, R. A., Koomen, M. J., et al. 1995, SoPh, 162, 357
Burlaga, L., Sittler, E., Mariani, F., & Schwenn, R. 1981, JGRA, 86, 6673
Carmichael, H. 1964, NASSP, 50, 451
Chen, P. F. 2011, LRSP, 8, 1
Colaninno, R. C., & Vourlidas, A. 2009, ApJ, 698, 852
Dryer, M., & Smart, D. 1984, AdSpR, 4, 291
Elliott, H. A., McComas, D. J., & DeForest, C. E. 2016, ApJ, 832, 66
Fry, C. D., Sun, W., Deehr, C. S., et al. 2001, JGR, 106, 20985
Gibson, S. E., & Low, B. C. 1998, ApJ, 493, 460
Gold, T., & Hoyle, F. 1960, MNRAS, 120, 89

Gopalswamy, N., Akiyama, S., Yashiro, S., & Xie, H. 2018a, in IAU Symp. 335, Space Weather of the Heliosphere: Processes and Forecasts (Cambridge: Cambridge Univ. Press), 258

Gopalswamy, N., Akiyama, S., Yashiro, S., & Xie, H. 2018b, JASTP, 180, 35

Gopalswamy, N., Lara, A., Manoharan, P. K., & Howard, R. A. 2005, AdSpR, 36, 2289

Gopalswamy, N., Lara, A., Yashiro, S., Kaiser, M. L., & Howard, R. A. 2001, JGR, 106, 29207

Gopalswamy, N., Mäkelä, P., Xie, H., & Yashiro, S. 2013, SpWea, 11, 661

Gopalswamy, N., Xie, H., Akiyama, S., Mäkelä, P. A., & Yashiro, S. 2014, EP&S, 66, 104

Gosling, J. T. 1990, GMS, 58, 343

Hickmann, K. S., Godinez, H. C., Henney, C. J., & Arge, C. N. 2015, SoPh, 290, 1105

Hirayama, T. 1974, SoPh, 34, 323

Hoeksema, J. T., Liu, Y., Hayashi, K., et al. 2014, SoPh, 289, 3483

Howard, R. A., Moses, J. D., Vourlidas, A., et al. 2008, SSRv, 136, 67

Hu, Q., Qiu, J., & Krucker, S. 2015, JGRA, 120, 5266

Isavnin, A. 2016, ApJ, 833, 267

Jin, M., Manchester, W. B., van der Holst, B., et al. 2017, ApJ, 834, 172

Jin, M., Schrijver, C. J., Cheung, M. C. M., et al. 2016, ApJ, 820, 16

Kaiser, M. L., Kucera, T. A., Davila, J. M., et al. 2008, SSRv, 136, 5

Kim, T. K., Pogorelov, N. V., Arge, C. N., et al. 2020, ApJS, 246, 40

Kim, T. K., Pogorelov, N. V., Borovikov, S. N., et al. 2014, JGRA, 119, 7981

King, J. H., & Papitashvili, N. E. 2005, JGRA, 110, A02104

Kopp, R. A., & Pneuman, G. W. 1976, SoPh, 50, 85

Linker, J. A., Caplan, R. M., Downs, C., et al. 2016, JPhCS, 719, 012012

Linker, J. A., Caplan, R. M., Downs, C., et al. 2017, ApJ, 848, 70

MacNeice, P., Elliott, B., & Acebal, A. 2011, SpWea, 9, S10003

Manchester, W. B., Gombosi, T. I., Roussev, I., et al. 2004, JGRA, 109, A02107

Marubashi, K. 2000, AdSpR, 26, 55

Mays, M. L., Taktakishvili, A., Pulkkinen, A., et al. 2015, SoPh, 290, 1775

McGregor, S. L., Hughes, W. J., Arge, C. N., Owens, M. J., & Odstrcil, D. 2011, JGRA, 116, A03101

Millward, G., Biesecker, D., Pizzo, V., & de Koning, C. A. 2013, SpWea, 11, 57

Moon, Y.-J., Dryer, M., Smith, Z., Park, Y. D., & Cho, K. S. 2002, GeoRL, 29, 1390

Murray, S. A. 2018, SpWea, 16, 777

Odstrcil, D., Riley, P., & Zhao, X. P. 2004, JGRA, 109, A02116

Pesnell, W. D., Thompson, B. J., & Chamberlin, P. C. 2012, SoPh, 275, 3

Pizzo, V. J., de Koning, C., Cash, M., et al. 2015, SpWea, 13, 676

Pogorelov, N., Borovikov, S., Heerikhuisen, J., et al. 2014, in Proc. 2014 Annual Conf. Extreme Science and Engineering Discovery Environment, XSEDE '14 22 (New York: ACM), 1

Qiu, J., Hu, Q., Howard, T. A., & Yurchyshyn, V. B. 2007, ApJ, 659, 758

Riley, P., Lionello, R., Mikić, Z., & Linker, J. 2008, ApJ, 672, 1221

Riley, P., Mays, M. L., Andries, J., et al. 2018, SpWea, 16, 1245

Sarkar, R., Gopalswamy, N., & Srivastava, N. 2020, ApJ, 888, 121

Schatten, K. H. 1971, CosEl, 2, 232

Schou, J., Scherrer, P. H., Bush, R. I., et al. 2012, SoPh, 275, 229

Scolini, C., Rodriguez, L., Mierla, M., Pomoell, J., & Poedts, S. 2019, A&A, 626, A122

Shen, C., Wang, Y., Pan, Z., et al. 2013, JGRA, 118, 6858

Shen, F., Feng, X. S., Wu, S. T., Xiang, C. Q., & Song, W. B. 2011, JGRA, 116, A04102

Shen, F., Shen, C., Zhang, J., et al. 2014, JGRA, 119, 7128

Shi, T., Wang, Y., Wan, L., et al. 2015, ApJ, 806, 271

Shiota, D., & Kataoka, R. 2016, SpWea, 14, 56

Singh, T., Kim, T. K., Pogorelov, N. V., & Arge, C. N. 2020, SpWea, 18, e02405

Singh, T., Yalim, M. S., & Pogorelov, N. V. 2018, ApJ, 864, 18

Singh, T., Yalim, M. S., Pogorelov, N. V., & Gopalswamy, N. 2019, ApJ, 875, L17

Singh, T., Yalim, M. S., Pogorelov, N. V., & Gopalswamy, N. 2020, ApJ, 894, 49

Song, H. Q., Zhang, J., Cheng, X., et al. 2020, ApJL, 901, L21

Sturrock, P. A. 1968, in IAU Symp. 35, Structure and Development of Solar Active Regions, ed. K. O. Kiepenheuer (Dordrecht: Reidel), 471

Temmer, M., Holzknecht, L., Dumbović, M., et al. 2021, JGRA, 126, e28380

Thernisien, A. 2011, ApJS, 194, 33

Thernisien, A., Vourlidas, A., & Howard, R. A. 2009, SoPh, 256, 111

Thernisien, A. F. R., Howard, R. A., & Vourlidas, A. 2006, ApJ, 652, 763

Titov, V. S., & Démoulin, P. 1999, A&A, 351, 707

Vandas, M., Fischer, S., Dryer, M., Smith, Z., & Detman, T. 1996, JGR, 101, 2505

Vandas, M., & Romashets, E. 2017, A&A, 608, A118

Verbeke, C., Pomoell, J., & Poedts, S. 2019, A&A, 627, A111

Vourlidas, A., Howard, R. A., Esfandiari, E., et al. 2010, ApJ, 722, 1522

Vršnak, B., & Gopalswamy, N. 2002, JGRA, 107, 1019

Vršnak, B., Temmer, M., Žic, T., et al. 2014, ApJS, 213, 21

Vršnak, B., & Zic, T. 2007, A&A, 472, 937

Wallace, S., Arge, C. N., Pattichis, M., Hock-Mysliwiec, R. A., & Henney, C. J. 2019, SoPh, 294, 19

Wang, Y. M., Ye, P. Z., Wang, S., Zhou, G. P., & Wang, J. X. 2002, JGRA, 107, 1340